

Article

Numerical Investigation of Fresh and Salt Water Distribution in the Pearl River Estuary during a Typhoon Using a Fully Coupled Atmosphere-Wave-Ocean Model

Jie Chen ^{1,2}, Changbo Jiang ^{1,2}, Zhiyuan Wu ^{1,2,3,4,*} , Yuannan Long ^{1,2}, Bin Deng ^{1,2} and Xiaojian Liu ⁴

¹ School of Hydraulic Engineering, Changsha University of Science & Technology, Changsha 410114, China; chenjie166@163.com (J.C.); jiangchb@csust.edu.cn (C.J.); longyuannan@163.com (Y.L.); dengbin07@csust.edu.cn (B.D.)

² Key Laboratory of Water-Sediment Sciences and Water Disaster Prevention of Hunan Province, Changsha 410114, China

³ School for Marine Science and Technology, University of Massachusetts-Dartmouth, New Bedford, MA 02744, USA

⁴ Key Laboratory of the Pearl River Estuarine Dynamics and Associated Process Regulation, Ministry of Water Resources, Guangzhou 510611, China; lxiaojian2010@163.com

* Correspondence: zwu@csust.edu.cn

Received: 15 January 2019; Accepted: 26 March 2019; Published: 28 March 2019



Abstract: Typhoons are major marine dynamic disasters that affect the coastal ocean areas of China. During a typhoon, the coupling dynamic factors, such as wind, waves, storm surges, and river runoff, greatly enhance the mass and energy exchange at the various interfaces of the ocean. A fully coupled atmosphere-wave-ocean model in the South China Sea (SCS) was established based on the WRF, SWAN, and ROMS models. The variation of sea surface salinity (SSS) and ocean subsurface salinity caused by Typhoon Kai-tak (201213) was analyzed by the fully coupled model, and the basic characteristics of the response of the upper ocean to the typhoon are given in this paper. The simulation results demonstrate that the salinity of the sea surface showed a sharp change during Typhoon Kai-tak, and it changed gradually after entering the recovery period. During the passage of Typhoon Kai-tak, the disturbance caused by strong winds strengthened the mixing process of the water in the Pearl River Estuary (PRE) and its adjacent waters. As the typhoon developed, under the influence of Ekman pumping, the mixing effect between the subsurface and the bottom and the upper water was obvious. Before the impact of Typhoon Kai-tak, the salinity had obvious stratification characteristics along the water depth. Due to the influence of the storm surge, the surface water with increased salinity was transported to the estuary, which led to an increase in the salinity of the estuary's surface water. In this condition, it is highly likely for there to be saltwater intrusion. The salinity distribution characteristics of three schemes (ROMS model only, coupled WRF-ROMS model, and fully coupled WRF-SWAN-ROMS model) were compared in this study. In the fully coupled WRF-SWAN-ROMS model, the disturbance of the bottom water was the most obvious, and the salinity value was greater than that of the coupled WRF-ROMS model, which indicates that under the influence of waves, the mixing and exchange abilities were strengthened.

Keywords: sea surface salinity (SSS); saltwater intrusion; storm surge; Pearl River Estuary; COAWST modeling system

1. Introduction

The typhoon is one of the most serious natural disasters that affects the coastal ocean environment in China [1–3], especially in the eastern and southern estuaries, such as the Yangtze River Estuary [4–6] and the Pearl River Estuary [7–9]. During a typhoon, the coupling of various dynamic factors, such as wind, waves, storm surges, and river runoff, greatly enhances the mass and energy exchange of various interfaces in the ocean and is accompanied by heavy rain and storm runoff on the surface [10]. Scouring can transport a large amount of minerals from the land to an estuary offshore, causing sudden changes in the water quality of the estuary, which may have an important impact on the marine ecological environment [1,9,11–13].

On the one hand, typhoon transit strengthens the mixing process of offshore water [14–16]. On the other hand, the heavy rainfall brought by a typhoon rapidly increases river runoff into the sea, and a large amount of land-based materials are washed away and brought into the estuary offshore area [17–20]. These changes due to the influence of a typhoon significantly affect the physical, chemical and biological processes of estuarine offshore waters, which in turn have an impact on the structure and function of the ecosystem [13,21–23]. Studying the changes of the estuarine nearshore environment under the influence of a typhoon and its ecological effects are of great importance for further understanding the evolution process of ecosystems in this region on a long-term scale [24,25].

Field observations show that the salinity of the surface water of an estuary usually shows a sharp change during a typhoon and the resulting rain, which gradually rises after entering the recovery period [26–28]. During typhoon crossing, the disturbance caused by strong winds strengthens the mixing process of the estuary and its adjacent waters [7,13]. However, this process has a passing impact on the water environment, and the runoff diluting water expansion and the external seawater intrusion play a greater role in changing the water environment after a typhoon. Among these, the strengthening of a typhoon after the expansion of fresh water greatly affects the upper water, the upper salinity decreases after the typhoon, and the nutrient salt concentration increases significantly. External seawater intrusion substantially changes the bottom water environment. The salinity of the bottom layer increases after a typhoon, and the nutrient concentration of nitrogen and silicon decreases.

Typhoons or tropical cyclones are strong wind events in the climate system and are a strong form of air-sea interaction. The strong vertical mixing and wind field generated by a typhoon has a major impact on the upper ocean dynamics and ecosystem [29]. Due to typhoons, there is a decrease in sea level, a decrease in sea surface temperature, an increase in phytoplankton blooms and a decrease in primary productivity, which also affect marine fisheries [30–32]. Typhoons mainly affect the marine ecological environment through two physical mechanisms: (1) after a typhoon, a cold vortex is formed, causing seawater to upwell and the lower layer of cold nutrient water is transported to the upper layer [33,34]; and (2) the typhoon intensifies the vertical mixing of the upper ocean by a strong wind process [35–38].

At present, most research on the sea surface salinity (SSS) response to typhoons is limited to the estuary area. According to the physical and biochemical environmental conditions of the estuary, SSS may show an upward or downward trend after typhoon transit [39–41]. However, studies on marine ecological factors, especially SSS and the response to typhoon transit, are limited and have not been discussed in detail [42–44]. The South China Sea (CSC) is the largest marginal sea in the Pacific Northwest, and is also a frequent typhoon zone, but it is difficult to obtain measured data during typhoons.

Due to the harsh meteorological conditions during typhoon transit, the use of on-site observation methods in an estuary to study the changes in the marine environment before and after a typhoon is very limited. The numerical simulation method is an effective way to study the distribution characteristics of fresh and salt water in an estuary under the influence of a typhoon.

In this study, a fully coupled atmosphere-wave-ocean model [1,7] was used to simulate the salinity changes in the upper ocean under the influence of a typhoon. The coupled WRF-SWAN-ROMS model in the South China Sea was established based on the model coupling toolkit (MCT), the mesoscale atmospheric model WRF, the wave model SWAN and the regional ocean model ROMS in this study.

The passage of Typhoon Kai-tak (201213) was observed in detail by a numerical model. Numerical observations revealed typhoon-induced sea surface salinity change. The typhoon wind and pressure field, typhoon waves, and storm surge under the influence of Typhoon Kai-tak were simulated based on this coupled model and some other coupled schemes. The characteristics of the atmospheric, wave and oceanic results in the South China Sea under the influence of this typhoon were calculated. The characteristics of surface salinity distribution and subsurface salinity distribution in the South China Sea during Typhoon Kai-tak were also analyzed in this study. The response of the upper ocean during Typhoon Kai-tak was studied to reveal the characteristics of SSS and subsurface salinity changes.

2. Model Setup and Case Study

2.1. Overview of Study Area

The South China Sea is a continental margin of Southeast Asia, which is part of the western Pacific Ocean and is the third continental margin of the world (Figure 1a). It covers an area of about 3.56 million km², and has an average water depth of about 1212 m. The deepest part is the central deep-sea plain, which reaches about 5567 m. In addition to being a main maritime transport route, the South China Sea is also rich in oil and natural gas. The Pearl River Delta (PRD) is a delta formed by the impact of the Xijiang River, Beijiang River, and Dongjiang River (Figure 1b). It covers an area of about 56,000 km² and is the second largest delta in China. The Pearl River Estuary (PRE) is the estuary where the delta network river and the remaining estuary bay coexist. The Pearl River Estuary has a large runoff, small tidal range and small concentration of sediment. The rivers in the Pearl River Estuary area develop a dense river network.

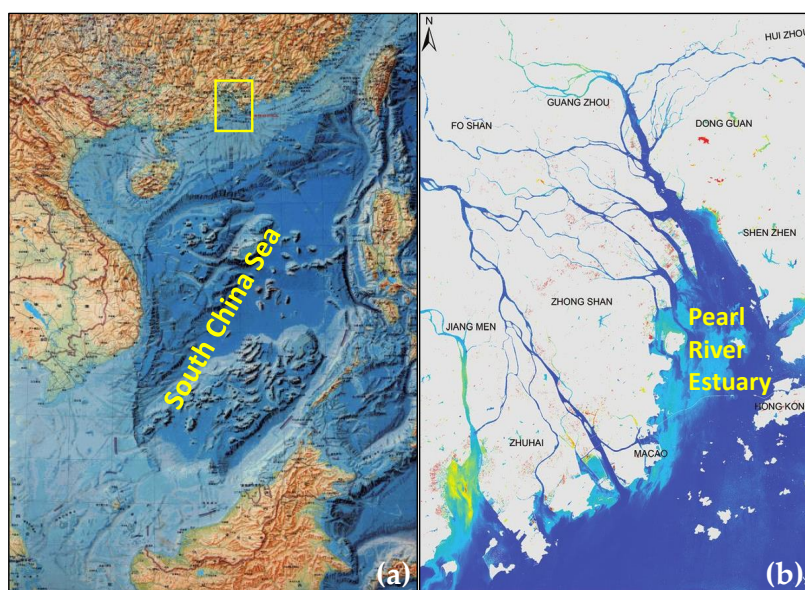


Figure 1. The geographical location of the study area: (a) the South China Sea; (b) the Pearl River Estuary.

The Pearl River Estuary system has eight radially distributed diverted waterways that flow into the South China Sea. The salt and fresh water near the estuary are generally mixed, and there is a strong mixing type in the dry season. The flood period is highly layered and there is an obvious salt wedge. The salt water in the dry season is far behind the Humen and Yamen waterways, and can reach Guangzhou, Zhongtang, Xinhui and other places in dry years.

Fresh water from the Pearl River Estuary spreads out to the South China Sea, and there are two axial directions. First, it is perpendicular to the coast and points to the southeast. In summer, it drifts to the northeast due to the influence of the southwest monsoon. It can expand to more than 100 km

away from Hong Kong during the flood period and shrink to the shore in winter and spring. Second, it is parallel to the coast year-round along the southwest. During the flood period, while the surface water of the offshore spreads to the South China Sea, there is deep shelf water offshore to compensate the movement along the coast. On average, there is one landfalling typhoon every year in the Pearl River Estuary, although there can be four or five in individual years. Affected by typhoons and tropical depressions, the estuary increases surge level significantly, with a maximum level increase of 1.58 m. During a typhoon, the maximum wave measured in Henglan Island (Hong Kong) was as high as 10.4 m.

2.2. Numerical Modeling: The COAWST Model System

The COAWST model system was presented and developed by Warner et al. [45,46] and includes the mesoscale atmospheric model WRF, the wave generation and propagation model SWAN, and the regional ocean model ROMS. The model coupled toolkit (MCT) as the coupler is used to exchange physical information between different model.

The fully coupled model was used to simulate Typhoon Kai-tak (201213). The simulation time includes the entire process of development and movement of Kai-tak in the South China Sea region (from 2012-08-15 00:00 to 2012-08-18 06:00). The simulation domains were the South China Sea and the nearby region (0°N , 102°S to 32°N , 130°S), as shown in Figure 2. The d01, d02, and d03 represent the three nesting domains of the WRF model, and the yellow and blue wireframes represent the parent and child simulation domains of the SWAN and ROMS, respectively. Specific configuration schemes for WRF, SWAN, and ROMS; initial conditions and boundary conditions; terrain elevation and grid configuration; etc., and verification of the model can be found in reference [1,7].

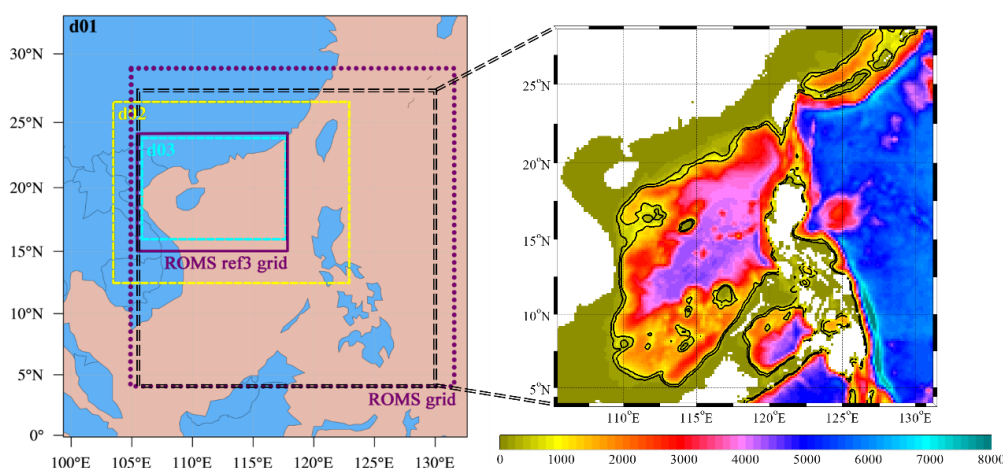


Figure 2. The simulation domain of the coupled WRF-SWAN-ROMS model in the South China Sea.

2.3. Computational Conditions

The fully coupled atmosphere-wave-ocean model of the South China Sea was established based on the WRF, SWAN, ROMS models and the MCT coupler in this study. The following were the physical exchanges between the models: (1) WRF to SWAN: 10-m wind speed (U_{10} , V_{10}); (2) SWAN to WRF: sea surface roughness simulated by wave height (H_s), wave length ($Len.$) and wave period ($Per.$); (3) WRF to ROMS: sea surface stress (τ), surface pressure, net heat fluxes, sensible heat flux, latent heat flux, shortwave radiation flux, and longwave radiation flux; (4) ROMS to WRF: sea surface temperature (SST); (5) SWAN to ROMS: wave height (H_s), wave direction ($Dir.$), wave length ($Len.$), wave period ($Per.$) and other wave parameters, and bottom orbital velocity; (6) ROMS to SWAN: topography, zeta, and depth-average velocity (u_a and v_a).

The simulation results of three different computational schemes (in Table 1) were used to compare and analyze the effects of the typhoon, surge and wave simulation results based on different coupling models, including:

(1) Run1 (Exp-ROMS): Only the ROMS model was used to simulate the oceanic results. This scheme was used to observe the salinity distribution characteristics under normal dynamic conditions (at the same time during Typhoon Kai-tak).

(2) Run2 (Exp-CWR): The coupled WRF and ROMS model was used to simulate the atmospheric and oceanic results of Typhoon Kai-tak. This scheme was used for the distribution of salinity in the South China Sea and the Pearl River Estuary without considering the wave dynamics under the influence of Typhoon Kai-tak.

(3) Run3 (Exp-CWSR): The fully coupled WRF, SWAN, and ROMS model was used to simulate the atmospheric, wave and oceanic results of Typhoon Kai-tak. This scheme was used for the distribution of salinity in the South China Sea and the Pearl River Estuary when considering the wave dynamics under the influence of Typhoon Kai-tak.

Table 1. The atmosphere-wave-ocean model considered in three different numerical schemes.

Run	Exps Name	WRF Model	SWAN Model	ROMS Model
R1	Exp-ROMS			✓
R2	Exp-CWR	✓		✓
R3	Exp-CWSR	✓	✓	✓

2.4. Selection of Typhoon: Kai-tak (201213)

Typhoon Kai-tak (201213) formed a tropical depression on the eastern sea of the Philippines on the evening of 12 August 2012 as shown in Figure 3. Kai-tak was a mild tropical cyclone that affected China, Vietnam, and Laos. It can be tracked back to the broad area of disturbance embedded in a monsoonal trough that was first spotted, early on 10 August 2012. It reached the southeast of Taiwan (16.9°N, 127.8°E) at about 08:00 on the 13th and continued to strengthen. The maximum wind speed reached 18 m/s or more, and the minimum air pressure was 998 hPa. At the same time, it moved northwestward at a speed of about 10 km/h and gradually approached the southern coast of Taiwan. The track of Typhoon Kai-tak is shown in Figure 3.

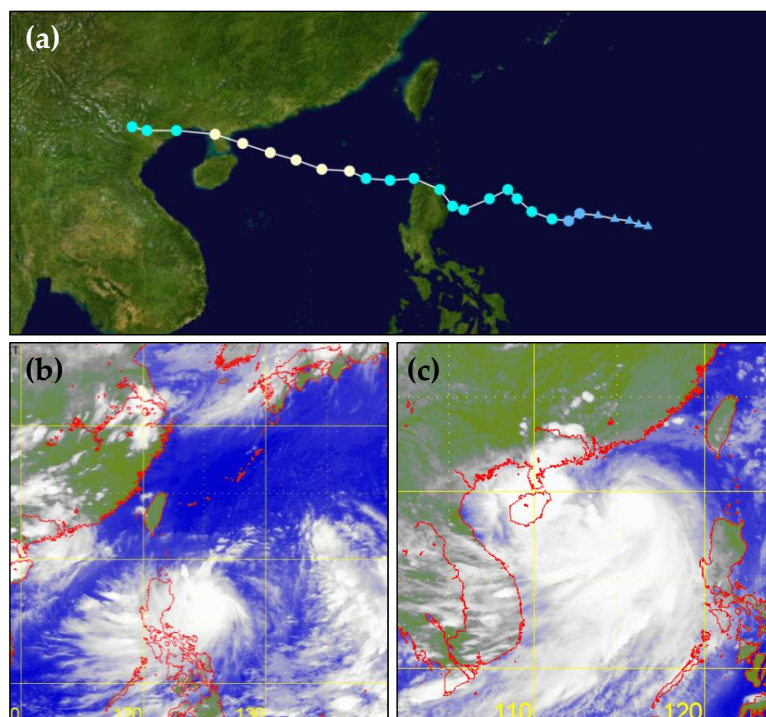


Figure 3. The track (a) and satellite images (b and c) of Typhoon Kai-tak (from the Hong Kong Observatory).

On 2012-08-16 05:00:00 UTC, it strengthened to the typhoon level over the north of the South China Sea. At 06:00 a.m., the center of the typhoon was south of Zhanjiang, Guangdong Province (18.7°N, 118.2°E). The maximum wind speed near the center was more than 33 m/s, and the minimum pressure in the center was 975 hPa. It made landfall on Zhanjiang in Guangdong Province at around 12:30 p.m. on 17 August 2012. At the time of landfall, the maximum wind speed near the center was 38 m/s, and the minimum pressure in the center was 968 hPa. At 21:30 on the 17th, it made landfall again on the China–Vietnam coast and began to weaken and gradually dissipated on the 18th. Typhoon Kai-tak caused heavy rainfall in most parts of southern China and caused floods and other disasters, killing 40 people and causing a total of US \$554.08 million in losses.

3. Results and Analysis

3.1. Sea Level Change Influenced by Astronomical Tide

For comparison with the ocean dynamics characteristics under the influence of a typhoon, the astronomical dynamic characteristics during the influence of Typhoon Kai-Tak were calculated and analyzed in this study. In this scheme (R1, ROMS model only), only the influence of the astronomical tide was considered, and the dynamic factors such as the atmosphere and waves (typhoon and waves) were not added.

Based on the R1 scheme (ROMS only), a three-dimensional ocean model over the South China Sea was established. According to the relevant parameter configuration, the tidal level change process in the South China Sea region from 2012-08-15 00:00 UTC to 2012-08-21 00:00 UTC was simulated. Figure 4 shows the simulated results of the astronomical tide level in the northern South China Sea during Typhoon Kai-tak from 2012-08-16 00:00 UTC to 2012-08-17 20:00 UTC.

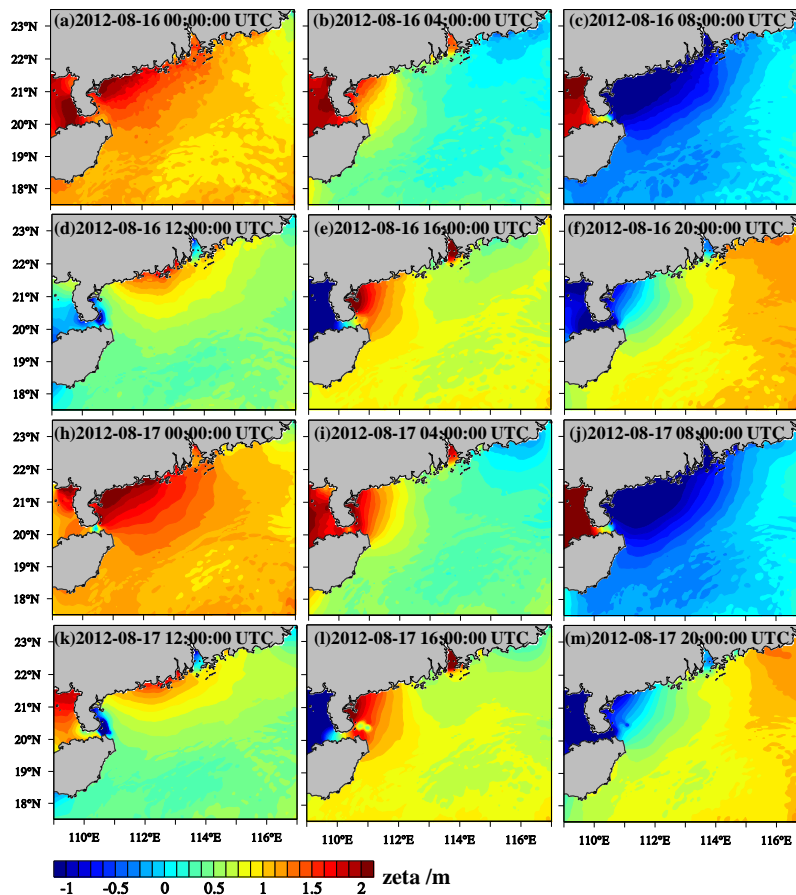


Figure 4. Astronomical tide level in the northern South China Sea during the Typhoon Kai-tak.

3.2. Salinity Distribution Driven by Astronomical Tide

Figure 5 shows the distribution of stratified salinity in the northern South China Sea, under only the astronomical dynamic forcing conditions during the Typhoon Kai-tak. It can be seen from Figure 5 that the surface salinity of the northern South China Sea was mainly distributed between 30 and 35 practical salinity units (PSU). The salinity of the Pearl River Estuary and its adjacent waters was relatively low less than 28 PSU, the surface salinity was low, and the bottom salinity was relatively large. According to the observations of the salinity distribution of the surface waters in the nearshore of the South China Sea in August 2012, it was found that the salinity in the estuary and nearshore areas was relatively low, especially in the Pearl River Estuary and its adjacent waters.

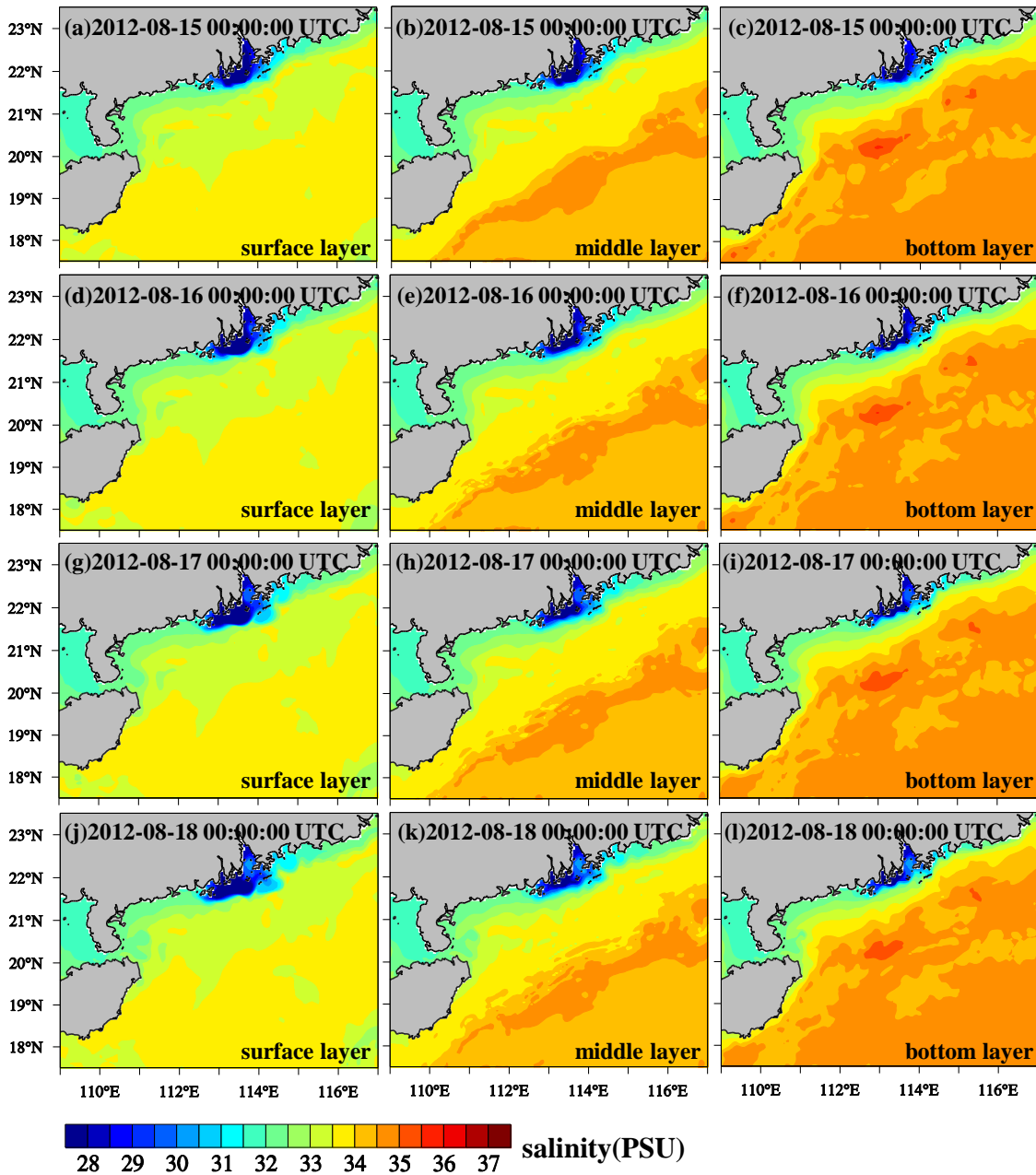


Figure 5. Distribution of salinity in the northern South China Sea under the influence of astronomical tide. PSU: practical salinity units.

The sea surface salinity of the five special positions was extracted based on the simulation results, and a time history curve was drawn, as shown in Figure 6. It can be seen from Figure 6 that the surface

salinity change of each special position was relatively small under the condition of astronomical dynamic forcing. Especially in the offshore zone (P3, P4, and P5), it was almost constant around 33.5 PSU. However, in the Pearl River Estuary zone (P2), the surface salinity underwent significant changes due to factors such as estuaries and nearshore dynamics.

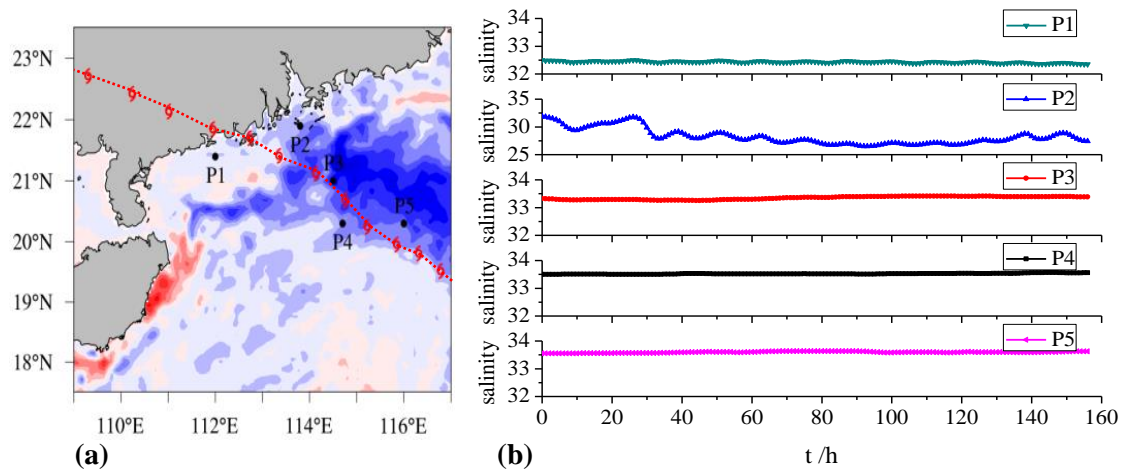


Figure 6. Surface salinity process of each special position (beginning on 2012-08-15 00:00:00 UTC): (a) special positions; (b) surface salinity at each position (unit: PSU).

3.3. Salinity Distribution Driven by Storm Surge

Under the influence of a typhoon, the salinity field will change significantly. Figure 7 shows the salinity field distribution of the surface, middle, and bottom layers of the northern South China Sea based on the fully coupled WRF-SWAN-ROMS model (R3 scheme, Exp-CWSR) during Typhoon Kai-tak. Figure 8 shows the changes in the salinity of the South China Sea before the impact of the typhoon based on the R3 scheme. The reference time is 2012-08-15 00:00 UTC.

It can be seen from Figure 8 that in the Pearl River Estuary and its adjacent coastal ocean, due to the influence of runoff and other dynamics factors, the salinity always remained relatively low, at about 28 PSU. During the influence of Typhoon Kai-tak, the low salinity waters of the Pearl River Estuary were brought to the southwest coast due to the influence of coastal ocean currents. It can be found that in the later stage of the influence of Typhoon Kai-tak, the salinity in the southwestern coastal ocean zone of the Pearl River Estuary decreased from about 33 to 31 PSU, and the salinity decreased by about 6.5% of the total salinity.

The change of salinity distribution was more obvious near the Pearl River Estuary during the influence of Typhoon Kai-tak. Figure 8a,d,g show that the surface salinity of the water in the upper ocean reaches of the Pearl River Estuary increased by about 1.5 PSU. From Figure 8c,f,i, it can be found that the salinity of the bottom of the water in the upper ocean reaches of the Pearl River Estuary is reduced by about 1.5 PSU. This indicates that, under the influence of storm surge, the bottom high salinity water was disturbed, and after exchange with the surface low salinity water, the surface water salinity increased. Due to the influence of storm surge, the surface water with increased salinity was transported to the estuary, which led to an increase in the salinity of the surface water of the estuary and a decrease in the salinity of the bottom layer. This condition is highly likely to cause saltwater intrusion.

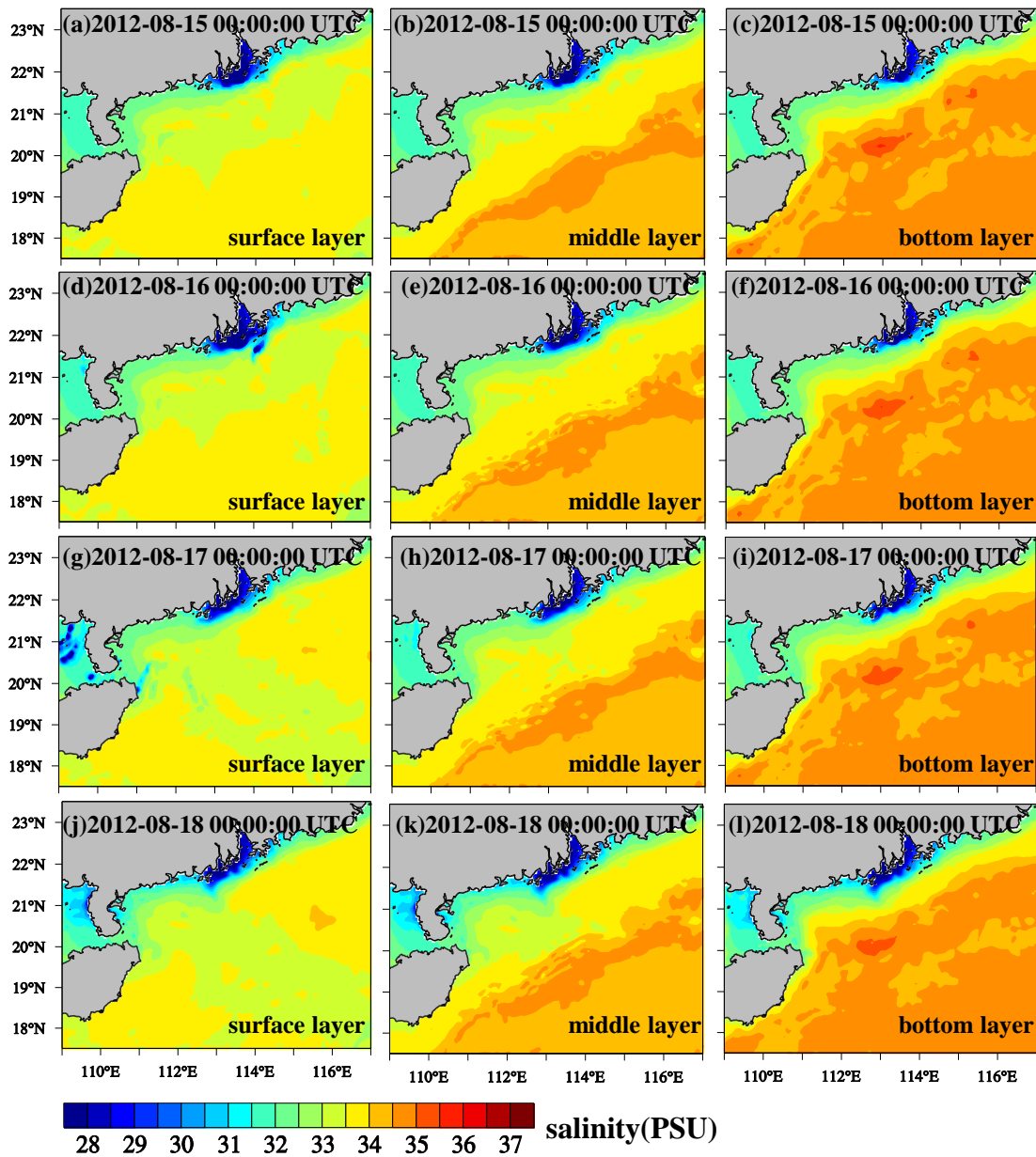


Figure 7. Temporal and spatial distribution of salinity fields under different stratifications influenced by Typhoon Kai-tak based on the fully coupled WRF-SWAN-ROMS model (R3 scheme, Exp-CWSR).

It can be seen from Figure 8a,d,g that the surface salinity of the upper ocean under the influence of this typhoon had asymmetrical distribution characteristics, which, on the right side of the typhoon track, was even more pronounced. On the right side of the typhoon track, the surface salinity increased by 1 PSU before the impact of the typhoon, while on the left side of the typhoon track, the surface salinity reduced by 1 PSU before impact. Under the influence of the typhoon, the bottom high-salinity water mixed with the surface low-salinity water under the upwelling flow process, resulting in an increase in surface salinity. On the left side of the typhoon track, due to the combined dynamics of wind-driven coastal currents and circulation (see Figure 9), the low-salinity water produced by the Pearl River runoff was transported to the left side of the typhoon track, resulting in a reduction in the salinity of the surface water on the left side of the track.

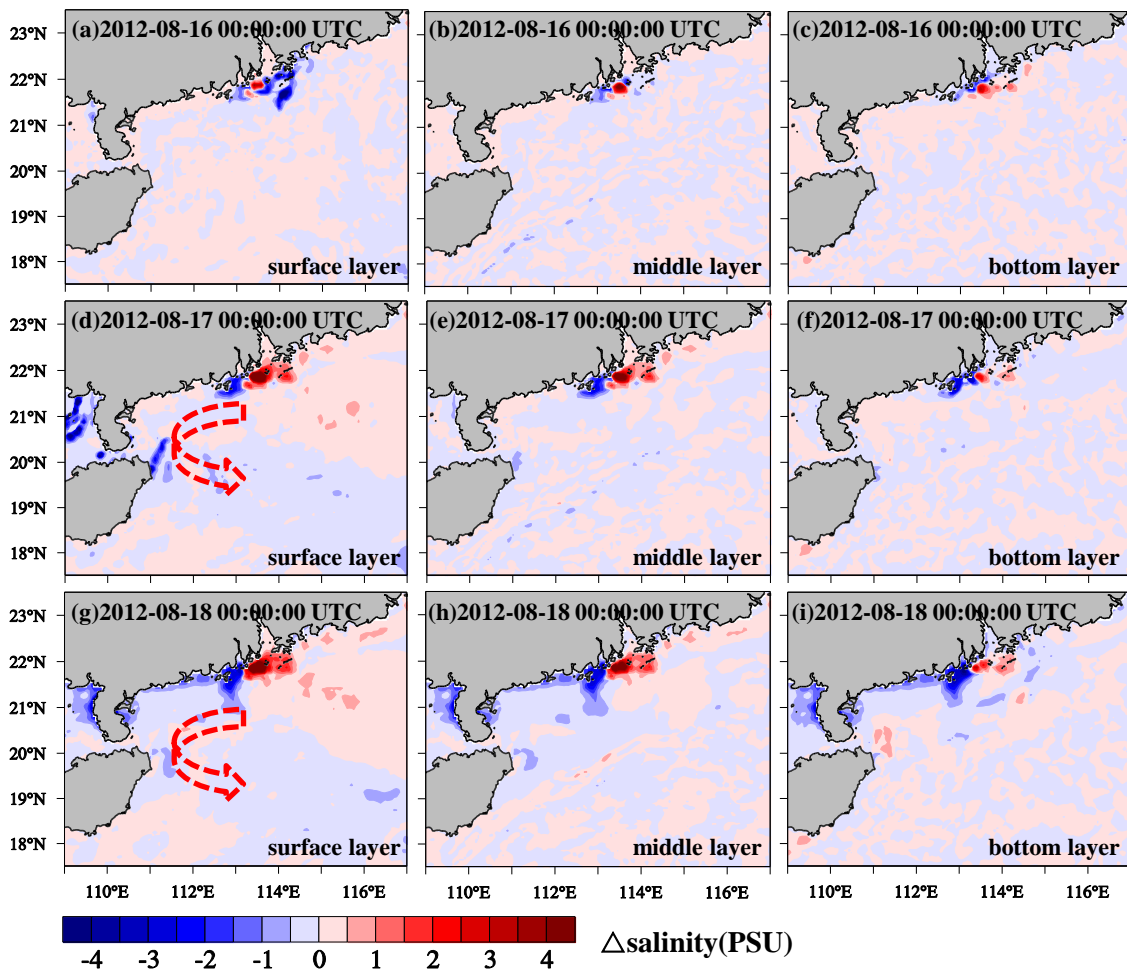


Figure 8. Changes in stratifications salinity influenced by Typhoon Kai-tak based on the fully coupled WRF-SWAN-ROMS model (beginning on 2012-08-15 00:00:00 UTC).

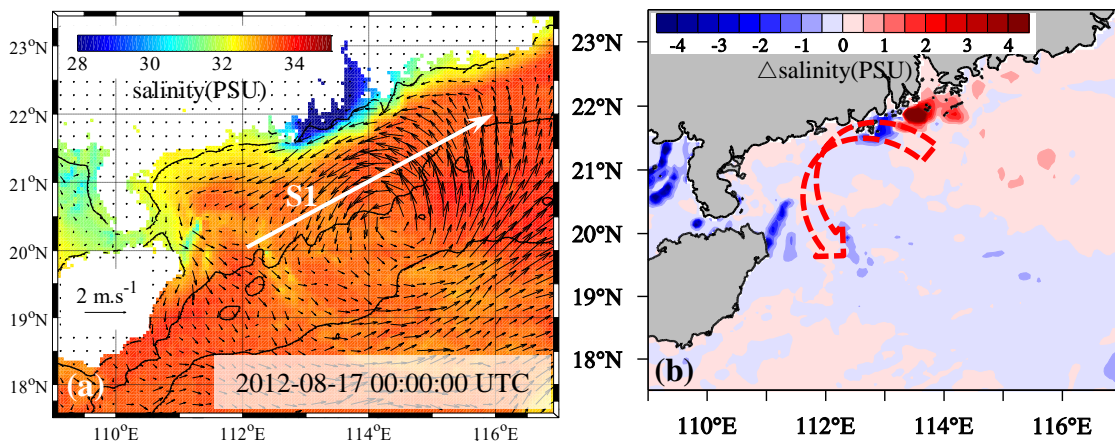


Figure 9. Influence of wind-driven circulation on salinity distribution during Typhoon Kai-tak. (a) flow field of wind-driven circulation; (b) change of salinity field.

Figure 10 shows the five special positions near the typhoon track (see Figure 6a) and the salinity of the surface, middle and bottom layers and local pressure at each position. From offshore to nearshore, the surface salinity at the P5 position (within the 1000-m isobath) increased by 0.5 PSU, and the salinity of the middle and bottom layers remained essentially unchanged. Due to the strong Ekman pumping of the ocean caused by the typhoon, the salinity at P4 (within the 200-m isobath) fluctuated under

strong mixing. Under the influence of Ekman pumping, the upper ocean was completely disturbed, and the salinity of the surface, middle and bottom layers and local pressure at P3 (within the 100-m isobath) had the same change trend as the sea surface salinity. The value of the middle salinity was close to the surface salinity. P1 and P2 were near the coast line, and due to the shallow depth of water, in the later stage of the typhoon, the salinity of the surface, middle and bottom layers in the whole section showed a similar trend.

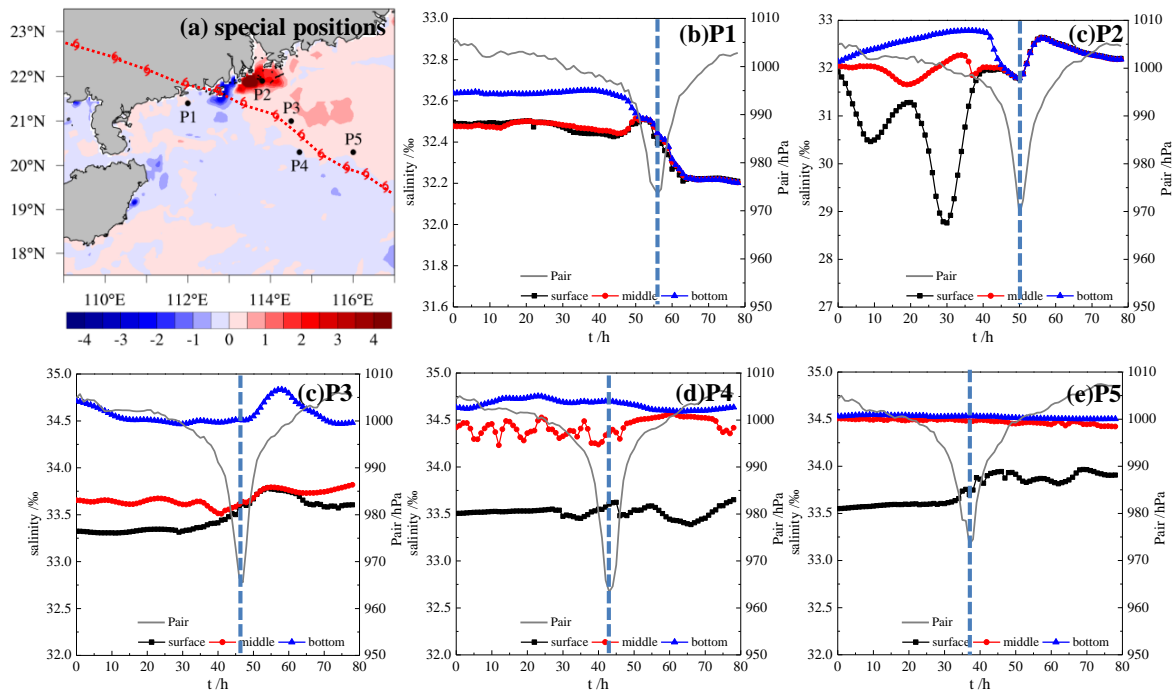


Figure 10. Variations in salinity of different layer at five different special positions (beginning on 2012-08-15 00:00:00 UTC).

It is worth noting that in the early stage of typhoon influence, due to the low-salinity water in the near estuary zone (P2), the salinity of the surface, middle and bottom layers was relatively close, at around 32 PSU. Under the influence of wind-driven circulation, the water on the east side of the Pearl River Estuary began to affect the west side of the estuary, resulting in a decrease in the salinity of the surface water at P2 and an increase in the salinity of the bottom layer. Under the action of the typhoon, the water body of the section was fully disturbed and had similar salinity and trends. In terms of time, the change of sea salinity was similar to the change of sea temperature [1,7], and it also lagged behind the moment when the extreme value of air pressure occurred, that is, the response of sea salinity to the typhoon had a time lag.

4. Discussions: Comparison of Salinity Distribution Under Different Coupling Schemes

In order to further explore the salinity distribution and variation characteristics of different depths of the upper ocean under the influence of a typhoon, the S1 section (shown in Figure 9a) was selected to plot the vertical distribution of salinity at different water depths. Figure 11a–d show the depth distribution of the salinity in the cross section at different times based on the R3 scheme (fully coupled WRF-SWAN-ROMS model, Exp-CWSR). Figure 11e,f show the depth distribution of the salinity in the cross section at different times based on the R2 scheme (coupled WRF-ROMS model, Exp-CWR).

From Figure 11a–d, it can be found that, as the typhoon developed, under the influence of Ekman pumping, the mixing action of the bottom and the surface water was obvious. It can be seen from the red dotted frame in the comparison chart that under the influence of the typhoon, the salinity of the water in different depths changed significantly. On 2012-08-15 00:00:00 UTC, before the impact of

Typhoon Kai-tak, it can be seen from Figure 11a that the salinity distribution characteristics along the water depth were more obvious. On 2012-08-17 00:00:00 UTC, after the impact of Typhoon Kai-tak, it can be seen from Figure 11c that the water above 60-m depth was disturbed, the salinity was relatively close, the overall salinity was around 33.7 PSU, and there were no longer any obvious layering characteristics.

From the comparison of Figure 11c–f, it can be found that the bottom water disturbance in the R3 scheme (fully coupled WRF-SWAN-ROMS model, Exp-CWSR) was more obvious than the water disturbance based on the R2 scheme (coupled WRF-ROMS model, Exp-CWR). In the black dotted frame in the figure, the salinity in this region was closer to the bottom salinity based on the R3 scheme (Exp-CWSR), and its value was greater than the salinity value based on the R2 scheme (Exp-CWR). This shows that the mixing ability with the upper ocean was strengthened under the influence of the waves' actions.

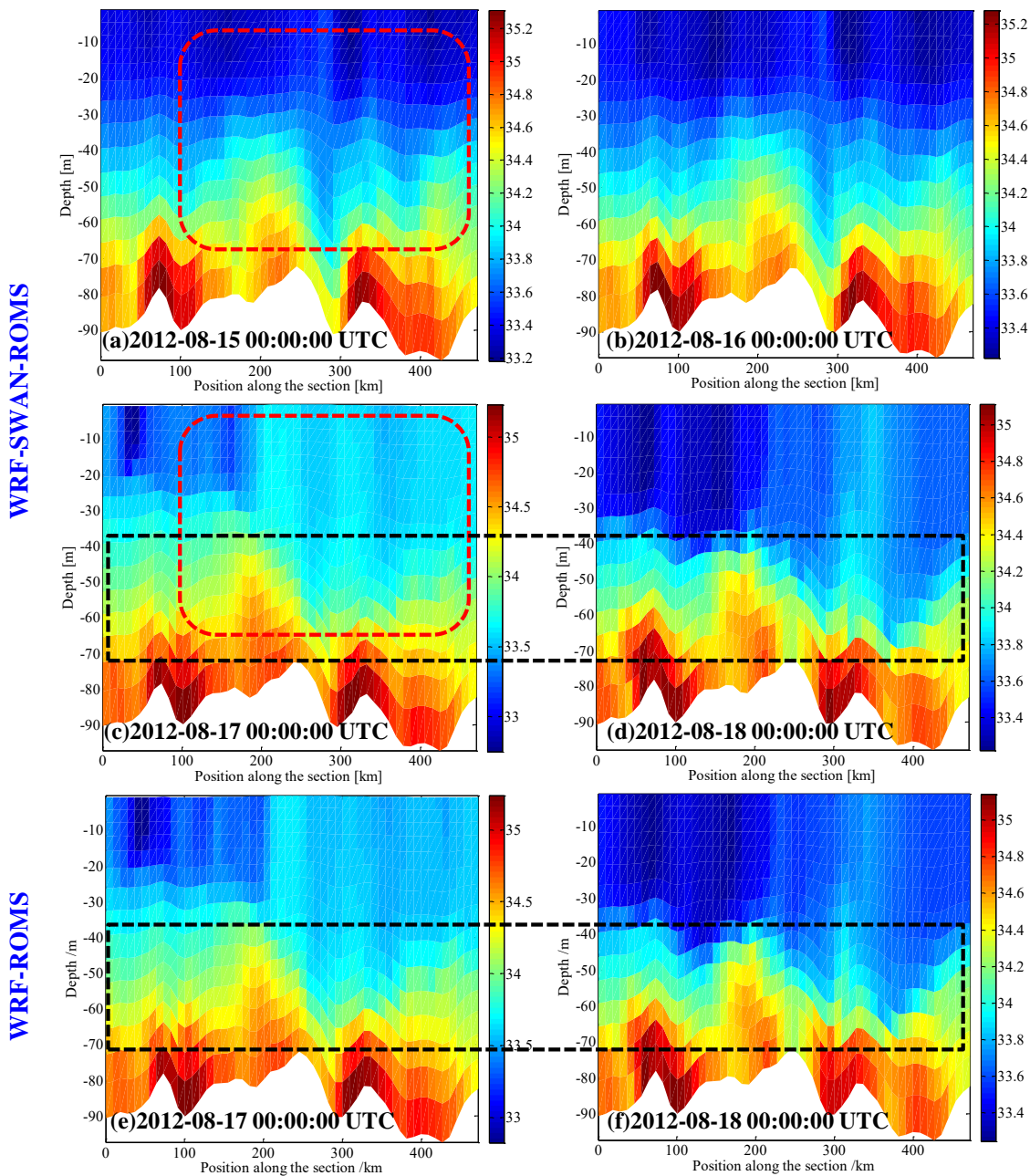


Figure 11. Distribution of salinity in the S1 section at different times in different coupling schemes.

The change in salinity of the surface, middle and bottom layers of the S1 section over time based on two different coupling schemes is shown in Figure 12. Overall, the distribution of salinity in different layers of the cross-section was similar in the two different coupling schemes. Comparing Figure 12a,b, it can be seen that the surface salinity simulated by the fully coupled scheme (R3, Exp-CWSR) was smaller than the surface salinity obtained by the R2 scheme (Exp-CWR).

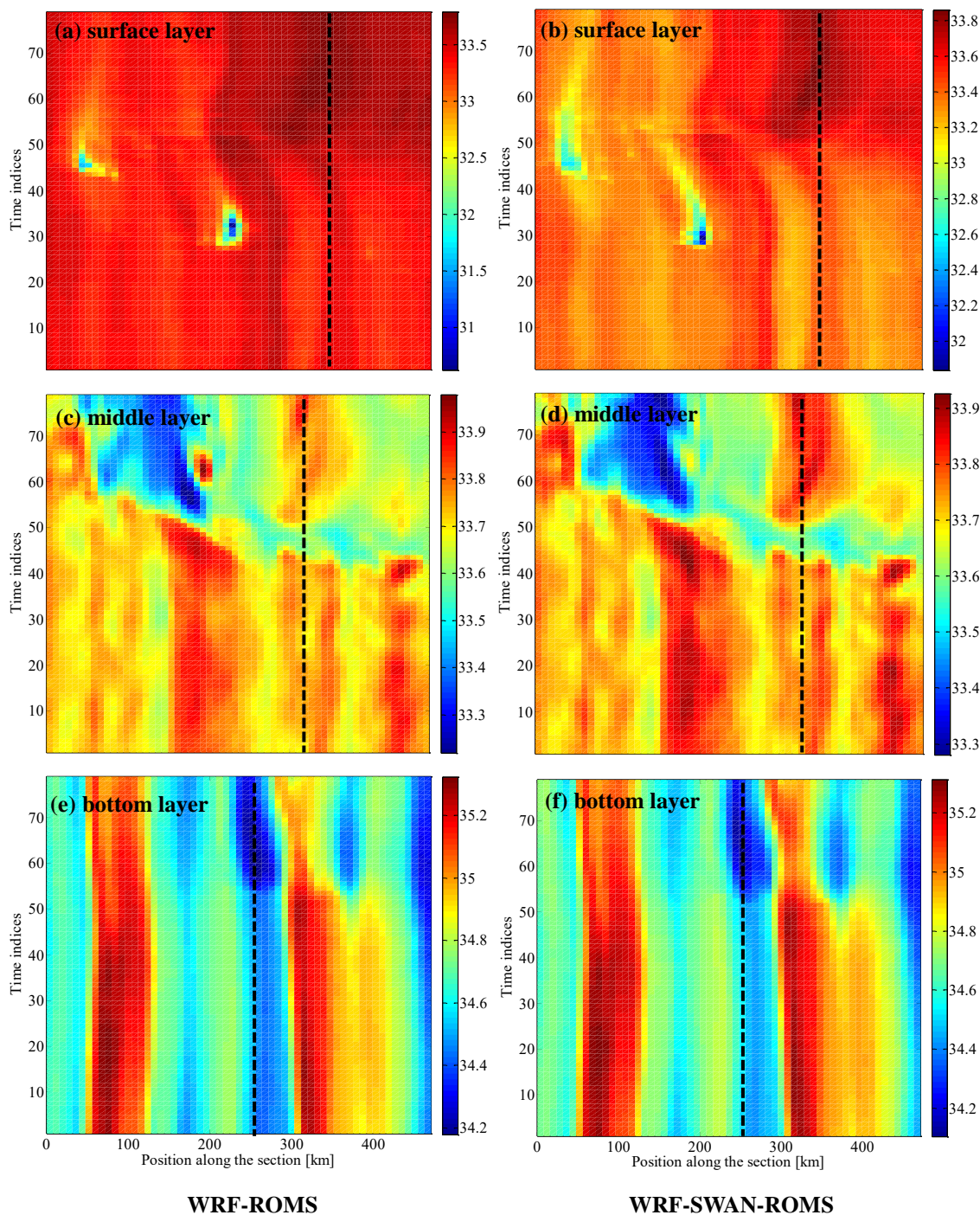


Figure 12. Comparison of different salinity layers of the S1 section in two different coupling schemes (beginning on 2012-08-15 00:00:00 UTC).

It can be seen from Figure 12c,d that the salinity of the middle water exhibited a two-step phenomenon, which first decreased and then increased. First, the salinity decreasing was due to

the strong Ekman pumping effect of the middle layer of water under the influence of the typhoon, which was mixed with the surface low-salinity water, resulting in a decrease in salinity. Secondly, as the Ekman pumping continued, an upwelling flow was created in the deeper water, resulting in an increase in the salinity of the middle seawater and a decrease in the salinity of the bottom water. This phenomenon was also reflected in Figure 12e,f.

Comparing the extreme value of the salinity change in the two different schemes (black vertical dotted line), it can be found that from the surface layer to the bottom layer, the extreme values of the salinity of each layer gradually approached the center of the typhoon based on the fully coupled scheme (R3, Exp-CWSR). That is, the asymmetric distribution of surface salinity based on the Exp-CWSR scheme was more obvious than that based on the Exp-CWR scheme, and the change of salinity on the right side of the typhoon track was significantly stronger than that of the left side. With the increase in water depth, the characteristics of this asymmetric distribution were gradually weakened.

5. Conclusions

In this study, fresh and salt water distribution model in the South China Sea during Typhoon Kai-tak was established to simulate the tide level, tidal current and salinity. The temporal and spatial distribution of sea salinity was simulated and discussed. The simulation results of three different coupled schemes were compared with the each other.

The following results were observed:

(1) The simulation results show that the salinity of the surface seawater showed a sharp change during Typhoon Kai-tak, and it changed gradually after entering the recovery period. During the passage of Typhoon Kai-tak, the disturbance caused by strong winds strengthened the mixing process of the water in the Pearl River Estuary and its adjacent waters, but the process had a limited impact on the ocean environment.

(2) As the typhoon developed, under the influence of Ekman pumping, the mixing effect between the subsurface and the bottom water and the upper water was obvious. Under the influence of the typhoon and storm surge, the salinity of the surface water increased due to the exchange of low-salinity water with the surface layer and the high-salinity water at the bottom layer by the disturbance processes.

(3) Due to the influence of the storm surge, the surface water with increased salinity was transported to the estuary, which led to an increase in the salinity of the surface water of the estuary. This condition is highly likely to cause saltwater intrusion.

(4) The salinity distribution characteristics of three schemes were compared in this study. In the fully coupled model (R3, Exp-CWSR), the disturbance of the bottom water was the most obvious, and the salinity value was greater than that in the coupled WRF-ROMS model (R2 scheme), which indicates that under the influence of waves, the mixing and exchange abilities were strengthened. During the influence of Typhoon Kai-tak, the low-salinity waters of the Pearl River Estuary were brought to the southwest coast due to the influence of coastal ocean currents. In the later stage of the influence of Typhoon Kai-tak, the salinity in the southwestern coastal ocean zone of the Pearl River Estuary decreased from about 33 to 31 PSU, and the salinity decreased by about 6.5% of the total salinity.

(5) Under the influence of the typhoon, the response of ocean salinity was characterized by asymmetric distribution and a delayed response. The response on the right side of the typhoon track was more pronounced than the response on the left side. The ocean salinity responded to the typhoons more than 6 h later than the pressure change, which was due to the time required for the mixing of the upper ocean.

There is another very important driving factor in the estuary area, which is runoff. In subsequent research, we will consider the combined effects of runoff, astronomical tides, and storm surges to study the fresh and salt water distribution in Pearl River Estuary under the combined influence of multiple extreme dynamic factors during a typhoon.

Author Contributions: J.C., C.J. and Z.W. prepared the original manuscript and designed the experiments; Y.L. and Z.W. made many modifications; B.D. and X.L. carried out the numerical experiments. All authors contributed to the analysis of the data and discussed the results.

Funding: This study was supported by the Open Research Foundation of Key Laboratory of the Pearl River Estuarine Dynamics and Associated Process Regulation, Ministry of Water Resources ([2018]KJ03). Partial support also came from the National Natural Science Foundation of China (Grant Nos. 51809023, 51839002, 51879015, 51879020 and 51809021), and the Key Laboratory of Water-Sediment Sciences and Water Disaster Prevention of Hunan Province (No. 2017SS04).

Conflicts of Interest: The authors declare no conflict of interests. The founding sponsors had no role in the design of the study; in the collection, analyses, or interpretation of data; in the writing of the manuscript, and in the decision to publish the results.

References

1. Wu, Z.; Jiang, C.; Chen, J.; Long, Y.; Deng, B.; Liu, X. Three-Dimensional Temperature Field Change in the South China Sea during Typhoon Kai-Tak (1213) Based on a Fully Coupled Atmosphere–Wave–Ocean Model. *Water* **2019**, *11*, 140. [[CrossRef](#)]
2. Zhang, Y.; Liu, L.; Bi, S.; Wu, Z.; Shen, P.; Ao, Z.; Chen, C.; Zhang, Y. Analysis of Dual-Polarimetric Radar Variables and Quantitative Precipitation Estimators for Landfall Typhoons and Squall Lines Based on Disdrometer Data in Southern China. *Atmosphere* **2019**, *10*, 30. [[CrossRef](#)]
3. Huang, C.; Hu, J.; Chen, S.; Zhang, A.; Liang, Z.; Tong, X.; Xiao, L.; Min, C.; Zhang, Z. How Well Can IMERG Products Capture Typhoon Extreme Precipitation Events over Southern China? *Remote Sens.* **2019**, *11*, 70. [[CrossRef](#)]
4. Dai, Z.; Liu, J.T.; Wei, W.; Chen, J. Detection of the Three Gorges Dam influence on the Changjiang (Yangtze River) submerged delta. *Sci. Rep.* **2014**, *4*, 6600. [[CrossRef](#)]
5. Guo, Y.; Zhang, J.; Zhang, L.; Shen, Y. Computational investigation of typhoon-induced storm surge in Hangzhou Bay, China. *Estuar. Coast. Shelf Sci.* **2009**, *85*, 530–536. [[CrossRef](#)]
6. Dai, Z.; Chu, A.; Li, W.; Li, J.; Wu, H. Has suspended sediment concentration near the mouth bar of the Yangtze (Changjiang) Estuary been declining in recent years? *J. Coast. Res.* **2013**, *29*, 809–818. [[CrossRef](#)]
7. Wu, Z.; Jiang, C.; Deng, B.; Chen, J.; Long, Y.; Qu, K.; Cao, Y. Numerical investigation of Typhoon Kai-tak (1213) using a mesoscale coupled WRF-ROMS model. *Ocean Eng.* **2019**, *175*, 1–15. [[CrossRef](#)]
8. Yin, K.; Xu, S.; Huang, W.; Xie, Y. Effects of sea level rise and typhoon intensity on storm surge and waves in Pearl River Estuary. *Ocean Eng.* **2017**, *136*, 80–93. [[CrossRef](#)]
9. Shen, Y.; Jia, H.; Li, C.; Tang, J. Numerical simulation of saltwater intrusion and storm surge effects of reclamation in Pearl River Estuary, China. *Appl. Ocean Res.* **2018**, *79*, 101–112. [[CrossRef](#)]
10. Bilskie, M.; Hagen, S.; Medeiros, S.; Cox, A.; Salisbury, M.; Coggin, D. Data and numerical analysis of astronomic tides, wind-waves, and hurricane storm surge along the northern Gulf of Mexico. *J. Geophys. Res.-Oceans* **2016**, *121*, 3625–3658. [[CrossRef](#)]
11. Fakour, H.; Lo, S.; Lin, T. Impacts of Typhoon Soudelor (2015) on the water quality of Taipei, Taiwan. *Sci. Rep.* **2016**, *6*, 25228. [[CrossRef](#)] [[PubMed](#)]
12. Wu, Z.; Jiang, C.; Deng, B.; Cao, Y. Simulation of the storm surge in the South China Sea based on the coupled sea-air model. *Chin. Sci. Bull.* **2018**, *63*, 3494–3504. [[CrossRef](#)]
13. Wang, T.; Liu, G.; Gao, L.; Zhu, L.; Fu, Q.; Li, D. Biological and Nutrient Responses to a Typhoon in the Yangtze Estuary and the Adjacent Sea. *J. Coast. Res.* **2015**, *32*, 323–332. [[CrossRef](#)]
14. Chen, Z.; Pan, J.; Jiang, Y.; Lin, H. Far-reaching transport of Pearl River plume water by upwelling jet in the northeastern South China Sea. *J. Mar. Syst.* **2017**, *173*, 60–69. [[CrossRef](#)]
15. Zhang, Z.; Wu, H.; Yin, X.; Qiao, F. Dynamics response of Changjiang River plume to a severe typhoon with the surface wave-induced mixing. *J. Geophys. Res.-Oceans* **2018**. [[CrossRef](#)]
16. Hu, J.; Wang, X. Progress on upwelling studies in the China seas. *Rev. Geophys.* **2016**, *54*, 653–673. [[CrossRef](#)]
17. Tsai, Y.; Chung, C.; Chung, C.; Gau, H.; Lai, W.; Liao, S. The Impact of Typhoon Morakot on Heavy Metals of Dapeng Bay and Pollution from Neighboring Rivers. *Environ. Model. Assess.* **2016**, *21*, 479–487. [[CrossRef](#)]
18. Jiang, C.; Wu, Z.; Chen, J.; Deng, B.; Long, Y. Sorting and sedimentology character of sandy beach under wave action. *Procedia Eng.* **2015**, *116*, 771–777. [[CrossRef](#)]

19. Jiang, C.; Wu, Z.; Chen, J.; Deng, B.; Long, Y.; Li, L. An available formula of the sandy beach state induced by plunging waves. *Acta Oceanol. Sin.* **2017**, *36*, 91–100. [[CrossRef](#)]
20. Huang, W. Modelling the effects of typhoons on morphological changes in the Estuary of Beinan, Taiwan. *Cont. Shelf Res.* **2017**, *135*, 1–13. [[CrossRef](#)]
21. Wu, X.; Wang, H.; Bi, N.; Song, Z.; Zang, Z.; Kineke, G. Bio-physical changes in the coastal ocean triggered by typhoon: A case of Typhoon Meari in summer 2011. *Estuar. Coast. Shelf Sci.* **2016**, *183*, 413–421. [[CrossRef](#)]
22. Wang, T.; Liu, G.; Gao, L.; Zhu, L.; Fu, Q.; Li, D. Biological responses to nine powerful typhoons in the East China Sea. *Reg. Environ. Chang.* **2017**, *17*, 465–476. [[CrossRef](#)]
23. Dai, Z.; Mei, X.; Darby, S.; Lou, Y.; Li, W. Fluvial sediment transfer in the Changjiang (Yangtze) river-estuary depositional system. *J. Hydrol.* **2018**, *566*, 719–734. [[CrossRef](#)]
24. Chen, N.; Krom, M.; Wu, Y.; Yu, D.; Hong, H. Storm induced estuarine turbidity maxima and controls on nutrient fluxes across river-estuary-coast continuum. *Sci. Total Environ.* **2018**, *628*, 1108–1120. [[CrossRef](#)]
25. Wu, Z.; Jiang, C.; Deng, B.; Chen, J.; Cao, Y.; Li, L. Evaluation of numerical wave model for typhoon wave simulation in South China Sea. *Water Sci. Eng.* **2018**, *11*, 229–235. [[CrossRef](#)]
26. Xu, J.; Wang, N.; Li, G.; Dong, P.; Li, J.; Liu, S.; Ding, D.; Wang, Z. The dynamic responses of flow and near-bed turbidity to typhoons on the continental shelf of the East China Sea: Field observations. *Geol. J.* **2016**, *51*, 12–21. [[CrossRef](#)]
27. Bernardo, L.; Nadaoka, K.; Nakamura, T.; Watanabe, A. Island-enhanced cooling mechanism in typhoon events revealed by field observations and numerical simulations for a coral reef area, Sekisei Lagoon, Japan. *Ocean Dyn.* **2017**, *67*, 1369–1384. [[CrossRef](#)]
28. Zhang, H.; Chen, D.; Zhou, L.; Liu, X.; Ding, T.; Zhou, B. Upper ocean response to typhoon Kalmaegi (2014). *J. Geophys. Res.-Oceans* **2016**, *121*, 6520–6535. [[CrossRef](#)]
29. Sun, J.; Oey, L.; Chang, R.; Xu, F.; Huang, S. Ocean response to typhoon Nuri (2008) in western Pacific and South China Sea. *Ocean Dyn.* **2015**, *65*, 735–749. [[CrossRef](#)]
30. Lin, I. Typhoon-induced phytoplankton blooms and primary productivity increase in the western North Pacific subtropical ocean. *J. Geophys. Res.-Oceans* **2012**, *117*, C03039. [[CrossRef](#)]
31. Liu, F.; Tang, S. Influence of the Interaction Between Typhoons and Oceanic Mesoscale Eddies on Phytoplankton Blooms. *J. Geophys. Res.-Oceans* **2018**, *123*, 2785–2794. [[CrossRef](#)]
32. Li, T.; Bai, Y.; He, X.; Chen, X.; Chen, C.-T.A.; Tao, B.; Pan, D.; Zhang, X. The Relationship between POC Export Efficiency and Primary Production: Opposite on the Shelf and Basin of the Northern South China Sea. *Sustainability* **2018**, *10*, 3634. [[CrossRef](#)]
33. Tsai, Y.; Chern, C.; Jan, S.; Wang, J. Numerical study of cold dome variability induced by Typhoon Morakot (2009) off northeastern Taiwan. *J. Mar. Res.* **2013**, *71*, 109–131. [[CrossRef](#)]
34. Li, D.; Huang, C. The Influences of Orography and Ocean on Track of Typhoon Megi (2016) Past Taiwan as Identified by HWRF. *J. Geophys. Res.-Atmos.* **2018**, *123*, 11–492. [[CrossRef](#)]
35. Wu, R.; Li, C. Upper ocean response to the passage of two sequential typhoons. *Deep-Sea Res. Part I* **2018**, *132*, 68–79. [[CrossRef](#)]
36. Yue, X.; Zhang, B.; Liu, G.; Li, X.; Zhang, H.; He, Y. Upper Ocean Response to Typhoon Kalmaegi and Sarika in the South China Sea from Multiple-Satellite Observations and Numerical Simulations. *Remote Sens.* **2018**, *10*, 348. [[CrossRef](#)]
37. Pujiana, K.; Moum, J.; Smyth, W. The Role of Turbulence in Redistributing Upper-Ocean Heat, Freshwater, and Momentum in Response to the MJO in the Equatorial Indian Ocean. *J. Phys. Oceanogr.* **2018**, *48*, 197–220. [[CrossRef](#)]
38. Zhang, X.; Chu, P.; Li, W.; Liu, C.; Zhang, L.; Shao, C.; Zhang, X.; Chao, G.; Zhao, Y. Impact of Langmuir Turbulence on the Thermal Response of the Ocean Surface Mixed Layer to Supertyphoon Haitang (2005). *J. Phys. Oceanogr.* **2018**, *48*, 1651–1674. [[CrossRef](#)]
39. Balaguru, K.; Foltz, G.; Leung, L.; Emanuel, K. Global warming-induced upper-ocean freshening and the intensification of super typhoons. *Nat. Commun.* **2016**, *7*, 13670. [[CrossRef](#)]
40. Lee, J.; Moon, I.; Moon, J.; Kim, S.; Jeong, Y.; Koo, J. Impact of typhoons on the Changjiang plume extension in the Yellow and East China Seas. *J. Geophys. Res.-Oceans* **2017**, *122*, 4962–4973. [[CrossRef](#)]
41. Nakada, S.; Kobayashi, S.; Hayashi, M.; Ishizaka, J.; Akiyama, S.; Fuchi, M.; Nakajima, M. High-resolution surface salinity maps in coastal oceans based on geostationary ocean color images: Quantitative analysis of river plume dynamics. *J. Oceanogr.* **2018**, *74*, 287–304. [[CrossRef](#)]

42. Rudzin, J.; Shay, L.; Johns, W. The influence of the barrier layer on SST response during tropical cyclone wind forcing using idealized experiments. *J. Phys. Oceanogr.* **2018**, *48*, 1951–1968. [[CrossRef](#)]
43. Lengaigne, M.; Neetu, S.; Samson, G.; Vialard, J.; Krishnamohan, K.; Masson, S.; Jullien, S.; Suresh, I.; Menkes, C. Influence of air–sea coupling on Indian Ocean tropical cyclones. *Clim. Dyn.* **2019**, *52*, 577–598. [[CrossRef](#)]
44. Steffen, J.; Bourassa, M. Barrier Layer Development Local to Tropical Cyclones based on Argo Float Observations. *J. Phys. Oceanogr.* **2018**, *48*, 1951–1968. [[CrossRef](#)]
45. Warner, J.C.; Sherwood, C.R.; Signell, R.P. Development of a three-dimensional, regional, coupled wave, current, and sediment-transport model. *Comput. Geosci.* **2008**, *34*, 1284–1306. [[CrossRef](#)]
46. Warner, J.C.; Armstrong, B.; He, R. Development of a Coupled Ocean–Atmosphere–Wave–Sediment Transport (COAWST) Modeling System. *Ocean Model.* **2010**, *35*, 230–244. [[CrossRef](#)]



© 2019 by the authors. Licensee MDPI, Basel, Switzerland. This article is an open access article distributed under the terms and conditions of the Creative Commons Attribution (CC BY) license (<http://creativecommons.org/licenses/by/4.0/>).